

This is the peer reviewed version of the following article:

Doping of III-V Arsenide and Phosphide Wurtzite Semiconductors / Giorgi, G.; Amato, M.; Ossicini, S.; Cartoixa, X.; Canadell, E.; Rurali, R.. - In: JOURNAL OF PHYSICAL CHEMISTRY. C. - ISSN 1932-7447. - 124:49(2020), pp. 27203-27212. [10.1021/acs.jpcc.0c09391]

*Terms of use:*

The terms and conditions for the reuse of this version of the manuscript are specified in the publishing policy. For all terms of use and more information see the publisher's website.

19/04/2024 00:05

(Article begins on next page)

1 **Doping of III–V Arsenide and Phosphide Wurtzite Semiconductors**2 Giacomo Giorgi,<sup>▽</sup> Michele Amato,<sup>▽</sup> Stefano Ossicini, Xavier Cartoixa, Enric Canadell,\*  
3 and Riccardo Rurali\*Cite This: <https://dx.doi.org/10.1021/acs.jpcc.0c09391>

Read Online

ACCESS |



Metrics &amp; More

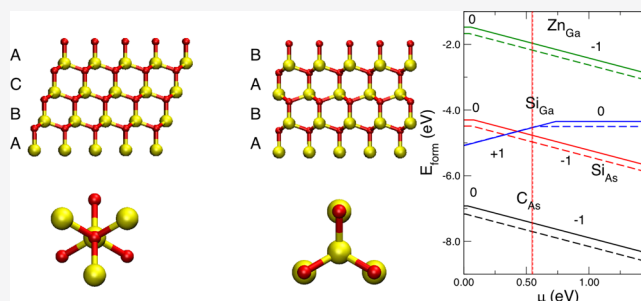


Article Recommendations



Supporting Information

4 **ABSTRACT:** The formation energies of n- and p-type dopants in  
5 III–V arsenide and phosphide semiconductors (GaAs, GaP, and  
6 InP) are calculated within a first-principles total energy approach.  
7 Our findings indicate that—for all the considered systems—both  
8 the solubility and the shallowness of the dopant level depend on the  
9 crystal phase of the host material (wurtzite or zincblende) and are  
10 the result of a complex equilibrium between local structural  
11 distortion and electronic charge reorganization. In particular, in the  
12 case of acceptors, we demonstrate that impurities are always more  
13 stable in the wurtzite lattice with an associated transition energy  
14 smaller with respect to the zincblende case. Roughly speaking, this  
15 means that it is easier to p-type dope a wurtzite crystal and the charge carrier concentration at a given temperature and doping dose  
16 is larger in the wurtzite as well. As for donors, we show that neutral chalcogen impurities have no clear preference for a specific  
17 crystal phase, while charged chalcogen impurities favor substitution in the zincblende structure with a transition energy that is  
18 smaller when compared to the wurtzite case (thus, charge carriers are more easily thermally excited to the conduction band in the  
19 zincblende phase).

20 **INTRODUCTION**

21 Crystal-phase engineering is an emerging field in nanoscience  
22 that consists of the design of materials with tailor-made  
23 properties by growing *ad hoc* crystal phases. The interest in this  
24 field was boosted by the enormous progresses made in recent  
25 years in the growth of semiconducting nanowires (NWs)<sup>1,2</sup>  
26 and, specifically, by the fact that metastable crystal phases,  
27 which in bulk can only be obtained under extreme conditions  
28 of temperature and pressure, can be stabilized at room  
29 temperature and atmospheric pressure, thanks to a tight  
30 control of growth conditions.<sup>3</sup> Many III–V semiconductors,  
31 such as arsenides<sup>4–7</sup> and phosphides,<sup>8–11</sup> that in bulk only  
32 exhibit the zincblende (ZB) phase, can take the wurtzite (WZ)  
33 structure when grown as NWs. Similarly, Si and Ge group-IV  
34 semiconductors that in bulk have the 3C cubic-diamond crystal  
35 structure can be synthesized in the 2H hexagonal-diamond  
36 (*i.e.*, lonsdaleite) polytype.<sup>12–15</sup> The possibility of growing  
37 semiconductors in different crystal phases is very appealing, as  
38 it might enable novel applications.<sup>16</sup> For instance, ZB GaP has  
39 an indirect band gap and thus a limited light emission  
40 efficiency, but in WZ GaP NWs, the band gap becomes direct,  
41 resulting in a strong photoluminescence.<sup>9</sup> Direct-band gap  
42 emission has also been predicted and reported in hexagonal Ge  
43 and SiGe alloys,<sup>17,18</sup> materials that have a notoriously poor  
44 light emission in the conventional cubic polytype adopted in  
45 the bulk. Moreover, in general, different polytypes can present  
46 different electronic,<sup>7,19–21</sup> optical,<sup>22–26</sup> and phononic proper-  
47 ties.<sup>27–31</sup>

Perhaps, the most ambitious (and exciting) goal of crystal-  
phase engineering is the design of complex structures by  
working only (or mostly) with different polytypes of the same  
material. The conditions that favor the formation of WZ over  
ZB segments in III–V NWs are well understood<sup>32–34</sup> and can  
be dynamically tuned during the growth. Therefore, not only  
isolated *homointerfaces* between the ZB and WZ crystal phase  
of a same material can be obtained<sup>22,35–37</sup> but also periodic  
superlattice structures can be obtained. In these crystal-phase  
superlattices, different polytypes of the same material—rather  
than different materials, like in conventional superlattices—are  
arranged periodically, building a metamaterial with its own  
unique properties, which can be tuned by controlling the  
number of periods and their thickness.<sup>38–41</sup> These crystal-  
phase interfaces present some advantages over the most  
common heterojunctions between two different materials: (i)  
they have a very small lattice mismatch and (ii) they have no  
chemical intermixing. As a result, they are atomically flat and  
virtually defect-free, which makes them ideal candidates to  
design materials with tailored electronic<sup>38,42,43</sup> and phononic<sup>67</sup>

Received: October 16, 2020

Revised: November 16, 2020

68 properties.<sup>44,45</sup> Similar effects have also been reported in the  
69 less-common crystal-phase core–multishell NWs.<sup>46,47</sup>

70 The vast majority of applications that can be envisaged in  
71 this context rely on impurity doping, which is the primary  
72 approach to tune the electrical conductivity of semiconductors.  
73 Indeed, the design of electronic devices is based on the  
74 juxtaposition of regions with different doping features, for  
75 example, in a pn junction, in a bipolar transistor or in a field-  
76 effect transistor. Therefore, a detailed understanding of doping  
77 in different crystal phases is necessary, both from the viewpoint  
78 of the fundamental understanding of the underlying physical  
79 mechanisms and for the operation of a multitude of  
80 applications. Given a material, is it equally easy to dope it in  
81 the ZB and WZ phase? Is the dopant activation energy the  
82 same or does it differ in different polytypes? The answers to  
83 these questions tell us how the solubility and the charge carrier  
84 concentration depend on the crystal phase and have thus far  
85 reaching consequences for the design and the optimization of  
86 any device.

87 In this paper, we study by means of first-principles electronic  
88 structure calculations of the doping of GaAs, GaP, and InP in  
89 the ZB and WZ crystal phase, considering a few common  
90 donor and acceptor impurities and an amphoteric impurity (Si  
91 in GaAs), whose doping type—donor or acceptor—depends  
92 on the sublattice where the substitution takes place. We  
93 consider both the neutral and singly charged impurity, thus  
94 allowing us to estimate the transition energy, that is, the  
95 shallowness of the dopant electron state, which determines the  
96 concentration of extrinsic charge carriers that are excited in the  
97 conduction or valence band for a certain doping dose and at a  
98 given temperature, and thus the electrical conductivity. We  
99 carry out our calculations in bulk systems, as a reasonable  
100 approximation of NWs with diameters of several tens of nm  
101 and where quantum confinement effects are negligible, which  
102 are commonly used in emergent electronic devices. We  
103 observe, nonetheless, that previous results obtained for Si  
104 showed that ultrathin NWs (diameters of ~2 nm) and bulk  
105 systems qualitatively exhibit the same behavior regarding the  
106 difference between the cubic and hexagonal crystal phase.<sup>43</sup>

## 107 ■ COMPUTATIONAL METHODS

108 **Electronic Structure Calculations.** We perform density  
109 functional theory (DFT) calculations with the VASP code<sup>48</sup>  
110 with the local density approximation (LDA) for the exchange–  
111 correlation energy functional. We used a plane wave cutoff  
112 ranging from 255.2 to 400 eV, depending on the atomic  
113 species involved, with the projector augmented-wave meth-  
114 od,<sup>49,50</sup> including semicore d electrons for Ga and In. At first,  
115 we optimized the lattice parameters of the ZB and WZ  
116 primitive cells, sampling the Brillouin zone with a  $10 \times 10 \times 10$   
117 and  $10 \times 10 \times 6$  grid of k-points, respectively. Our results are  
118 shown in Table 1. Substitutional impurities at both the group-  
119 III and group-V sublattice were studied in  $5 \times 5 \times 5$  and  $5 \times 5$   
120  $\times 3$  supercells of the 2- and 4-atom ZB and WZ primitive cells,  
121 with a  $2 \times 2 \times 2$  grid of k-points. The geometry of the doped  
122 supercells was optimized with a quasi-Newton algorithm until  
123 all the forces on the atoms were lower than 0.01 eV/Å. This  
124 computational setup proved to be accurate enough to give  
125 converged values of the formation energy, as shown in previous  
126 theoretical studies.<sup>51–54</sup>

127 We also used density functional perturbation theory  
128 (DFPT) to compute the macroscopic dielectric tensor,  
129 explicitly accounting for local field effects, which is needed

**Table 1. Lattice Parameters, Relative Dielectric Constants, and  $G_0W_0$  Band gaps (LDA Values are Indicated in Parenthesis)**

		$a$ (Å)	$c$ (Å)	$\epsilon_{xx}$	$\epsilon_{zz}$	bandgap (eV)
GaAs	zincblende	5.601		13.75	13.75	1.66 (0.54)
	wurtzite	3.946	6.510	12.80	13.03	1.46 (0.55)
GaP	zincblende	5.381		10.52	10.52	2.17 (1.39)
	wurtzite	3.790	6.254	10.16	10.60	2.28 (1.32)
InP	zincblende	5.821		11.41	11.41	1.42 (0.62)
	wurtzite	4.107	6.748	10.73	10.96	1.49 (0.68)

for the charge correction scheme described below. We used the  
optimized lattice vectors and atomic positions obtained at the  
single-particle DFT level. The computational parameters are  
the same as for the DFT calculations, but we found that greatly  
increased k-point meshes are needed to obtain converged  
results. We used a  $36 \times 36 \times 36$  and  $36 \times 36 \times 22$  grid for the  
ZB and WZ polytypes, respectively. The results are  
summarized in Table 1.

On top of the previously optimized primitive cells, we  
performed *single-shot*  $G_0W_0$  calculations, where quasiparticle  
energies are calculated from a single GW iteration, that is, using  
the screened potential ( $W$ ) as obtained from the DFT (LDA)  
step. To improve the quality of the results, a large number of  
real frequency points (200) have been employed for the  
Hilbert transform of  $W$  and self-energy,  $\Sigma$ . Similarly, a very  
large number of empty bands (~200) have been included in  
the calculations to ensure convergence of the results.

**Handling of Computational Cells with Net Charge.**  
Plane-wave DFT codes, but also localized basis set codes with  
a Poisson solver based on reciprocal space, assume that the  
system extends *ad infinitum* with the periodicity set at the  
input for the computational cell. For charge-neutral systems,  
this use of periodic boundary conditions (PBCs) is of course  
well justified in bulk 3D systems, and in lower dimensionalities,  
it poses no special difficulties, provided that a thick-enough  
vacuum buffer is added to prevent the interaction between the  
(spurious) system replicas.

The situation is, however, different when addressing systems  
with isolated net charges, such as the case with an ionized  
dopant of interest to us here. The long-range Coulomb  
interaction between the PBC-induced charge replicas will  
introduce a spurious contribution to the total energy that must  
be corrected for. Several correction schemes have been  
proposed<sup>55–58</sup> (see also ref 59 and references therein), often  
involving the computation of the Madelung energy for some  
geometric arrangement of point charges in a compensating  
background.<sup>60,61</sup> In this work, we use a variant of the Makov–  
Payne scheme<sup>56</sup> that some of us extended to the case of the  
arbitrary shape of the computational cell and tensor value of  
the dielectric constant,<sup>62</sup> which is necessary for the hexagonal  
cells in the WZ case. This type of correction was shown to  
accelerate convergence in the case of NWs,<sup>63</sup> and thus, it is  
also expected to do it here.

The elements of the dielectric tensor that we have used for  
our Madelung correction have been obtained from a DFPT  
calculation as detailed above. We do not consider it necessary  
to correct these dielectric tensor entries with their  
experimental counterparts, given that the interaction between  
the point charge replicas will be screened according to our  
used theory level, that is, LDA.

180 **Formation Energy.** The formation energy is the central  
181 quantity in defect analysis and it tells us how likely it is to  
182 observe a defect in a crystal matrix,<sup>59</sup> either in the case of  
183 intrinsic imperfections of the crystal lattice or—the case  
184 addressed here—when it comes to an impurity added on  
185 purpose to alter in a controlled way the property of a material.  
186 The knowledge of the formation energy of a defect delivers  
187 some important information concerning the impurity equi-  
188 librium concentrations,<sup>64–66</sup> the solubilities,<sup>67,68</sup> or the  
189 diffusivities.<sup>69,70</sup> Additionally, by comparing the formation  
190 energy of a neutral and singly charged defect, one can obtain  
191 the transition energy, a quantity of paramount importance in  
192 semiconductor physics that tells us which is the energy needed  
193 to thermally excite carriers from the dopant state to the  
194 conduction or valence band. The formation energy, as  
195 introduced by Zhang and Northrup,<sup>64</sup> is written as follows

$$E_{\text{form}} = E_{\text{tot}}^{\text{D}} - \sum_i n_i \mu_i + q(\mu_e + E_V) \quad (1)$$

196 where  $E_{\text{tot}}^{\text{D}}$  is the total energy of the system including the defect,  
197 the sum runs over all the chemical species present, and  $n_i$  and  
198  $\mu_i$  are the number of atoms and chemical potential of species  $i$ ,  
199 respectively.  $q$  is the charge state of the defect and  $\mu_e$  is the  
200 chemical potential of the electron, which is referred to as  $E_V$ ,  
201 the highest occupied eigenvalues of the pristine system.  
202 Therefore,  $\mu_e$  varies from 0—at the top of the valence  
203 band—to  $E_{\text{gap}}$ —at the bottom of the conduction band—thus  
204 spanning the whole range of doping conditions.

205 In the case of a compound semiconductor like the ones  
206 studied in this work, eq 1 is conveniently reformulated as<sup>65</sup>

$$E_{\text{form}} = E_{\text{D}}^{\text{tot}} - \frac{1}{2}(n_{\text{Ga}} + n_{\text{As}})\mu_{\text{GaAs}}^{\text{bulk}} - \frac{1}{2}(n_{\text{Ga}} - n_{\text{As}}) \\ (\mu_{\text{Ga}}^{\text{bulk}} - \mu_{\text{As}}^{\text{bulk}} + \Delta\mu) + \\ q(\mu_e + E_V) - n_X \mu_X \quad (2)$$

208 which, for simplicity, is written for the case of GaAs with a  
209 generic impurity X. The chemical potentials  $\mu_{\text{Ga}}^{\text{bulk}}$ ,  $\mu_{\text{As}}^{\text{bulk}}$ , and  
210  $\mu_{\text{GaAs}}^{\text{bulk}}$  refer to the bulk compound of Ga, As, and GaAs. We  
211 computed  $\mu_{\text{Ga}}^{\text{bulk}}$  and  $\mu_{\text{As}}^{\text{bulk}}$  as the energy per atom of Ga and As  
212 in the orthorhombic and trigonal phase, respectively; for  $\mu_{\text{GaAs}}^{\text{bulk}}$ ,  
213 we considered the ZB or WZ crystal phase, depending on the  
214 case being addressed. Note that  $\mu_{\text{Ga}}$  and  $\mu_{\text{As}}$  are the chemical  
215 potential of Ga and As in GaAs, respectively, and that  
216 computing their value is not straightforward. However, one can  
217 observe that the chemical potential of bulk GaAs is  $\mu_{\text{GaAs}}^{\text{bulk}} =$   
218  $\mu_{\text{Ga}}^{\text{bulk}} + \mu_{\text{As}}^{\text{bulk}} - \Delta H_f$ , where  $\Delta H_f$  is the heat of formation of  
219 GaAs. Now,  $E_{\text{form}}$  is a function of the bulk chemical potential of  
220 Ga and As and of the parameter  $\Delta\mu$  that accounts for the  
221 difference between the chemical potentials of Ga and As in  
222 GaAs and in their respective bulk state. The reformulation of  
223  $E_{\text{form}}$  in eq 2 has the advantage of expressing it in terms of well-  
224 defined quantities (the bulk chemical potentials) and of the  
225 parameter

$$\Delta\mu = (\mu_{\text{Ga}} - \mu_{\text{As}}) - (\mu_{\text{Ga}}^{\text{bulk}} - \mu_{\text{As}}^{\text{bulk}}) \quad (3)$$

226 which accounts for the macroscopic stoichiometry conditions  
227 of the material.  $\Delta\mu$  can vary between  $-\Delta H_f$ , the limit that  
228 corresponds to the As-rich conditions, and  $\Delta H_f$  for the Ga-  
229 rich material, conditions fixed by the inequalities  $\mu_{\text{Ga}} \leq \mu_{\text{Ga}}^{\text{bulk}}$

and  $\mu_{\text{As}} \leq \mu_{\text{As}}^{\text{bulk}}$ . This formalism is also applied to the case of  
230 GaP and InP, where we considered the cubic phase for bulk P  
231 and the trigonal phase for bulk In to define  $\mu_{\text{P}}^{\text{bulk}}$  and  $\mu_{\text{In}}^{\text{bulk}}$ ,  
232 respectively.

233 In the case of the chemical potential of the dopant,  $\mu_X$  ( $X =$   
234 Si, C, Zn, S, and Te), we have taken the energy of the isolated  
235 atom, assuming that the impurity is incorporated into the  
236 crystal from the gas phase. This choice, although sound, is an  
237 approximation, because the chemical reservoir where the  
238 impurity comes from is not necessarily the one of a  
239 monoatomic gas. A different choice would result in a different  
240 value of the formation energy (see, e.g., ref 71 for a discussion  
241 of the case of H in SiC). Notice, however, that whenever we  
242 compare the formation energy of a given impurity in the ZB or  
243 WZ crystal phase,  $\mu_X$  cancels out and thus, the conclusions do  
244 not depend on its exact value, as already shown in refs 53, 54.  
245 The same happens when comparing the formation energy of a  
246 dopant in the neutral and singly charged state, which  
247 determines the transition energy (neither the transition energy  
248 depends on  $\mu_X$ ).  
249  
250  
251

## RESULTS AND DISCUSSION

### Stability and Band gap of the Pristine Bulk Systems.

252 Before discussing impurity doping, it is instructive to revise the  
253 theory that explains why a given semiconductor adopts one  
254 crystal structure or the other, as it will then be important to  
255 understand the stability of dopants as well. The simplest way to  
256 understand the difference between the ZB and WZ crystal  
257 phases is by looking at the stacking sequence along the [111]  
258 cubic axis, which is equivalent to the [0001] axis of the WZ. As  
259 it is easy to see in Figure 1a,b, in the ZB crystal structure, the  
260  
261

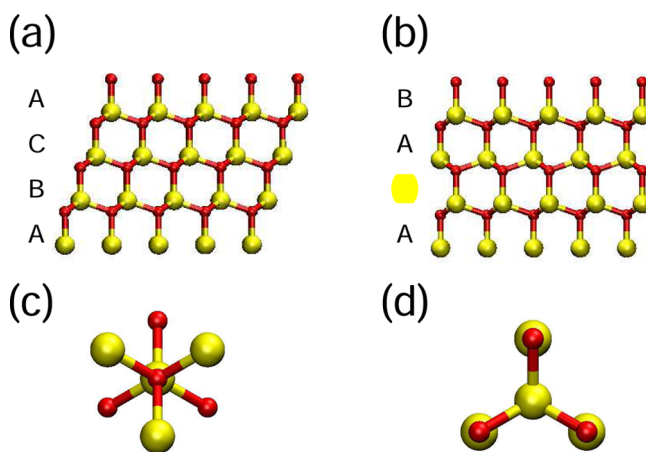


**Figure 1.** Side view of (a) ZB and (b) WZ lattice structure where the ABCABC vs ABABAB stacking along the cubic [111] axis can be appreciated. (c) Staggered and (d) eclipsed dihedral conformation of the ZB and WZ crystal phases.

262 III–V bilayers are stacked one on top of the other according to  
263 an ABCABC stacking motif, while in the WZ one, they follow  
264 an ABABAB stacking sequence. When III-arsenides or III-  
265 phosphides form, the starting point is always the AB stacking,  
266 as the sequence of two bilayers of the same type, for example,  
267 AA, is energetically unfavorable. When the next layer grows, it  
268 can take the A or C position and thus the ZB or WZ symmetry.  
269 In other words, the two polytype structures differ only in the  
270 eclipsed (WZ) or staggered (ZB) dihedral conformation that  
271 in turn affects the 1,4 atomic interactions (see in Figure 1c,d).  
272  
273

272 Under such conditions, the preference for one of the two  
273 crystal phases is the result of a competition between covalent  
274 and ionic contributions.<sup>72,73</sup> For compounds following the  
275 octet rule,  $A^N B^{8-N}$ , the WZ structure is favored when the ionic  
276 component is strong. The limiting case is constituted by group-  
277 IV semiconductors, that is, Si, Ge, and diamond, where the  
278 bond is fully covalent and that accordingly adopt the cubic  
279 structure. Then, in III–V semiconductors, the larger the ionic  
280 contribution is, the less the ZB phase will be favored over the  
281 WZ one, until the latter becomes the ground state as in GaN.

282 Our results agree well with this picture, as we found that the  
283 preference for the ZB structure according to our calculations is  
284 21.9 meV for GaAs, 17.4 meV for GaP, and 10.6 meV for InP  
285 per unit formula (f.u.), which follows a prediction based on the  
286 electronegativity differences between the anion and cation  
287 according to the Pauling scale, a crude measure of the ionicity  
288 of the bond: 0.37 for GaAs, 0.38 for GaP, and 0.41 in InP.  
289 Therefore, the larger the electronegativity difference is, the  
290 more ionic is the bond and the less favored is the ZB crystal  
291 phase. A more refined definition of the ionicity of a bond is the  
292 so-called atomic asymmetry parameter (AAS) between a pair  
293 of atoms,<sup>74,75</sup> which is known to work well in crystals of the  
294  $A^N B^{8-N}$  type. The AAS values for GaAs, GaP, and InP are  
295 0.316, 0.371, and 0.506, respectively, which are also in good  
296 agreement with the abovementioned energy preferences. Other  
297 criteria to estimate the ionic character of the chemical bond are  
298 of course possible; see, for example, the ionicity scale based on  
299 the centers of maximally localized Wannier functions of Abu-  
300 Farsakh and Qteish.<sup>76</sup>

301 One of the reasons of interest in crystal-phase engineering is  
302 the tunability of the electronic properties. Therefore, another  
303 issue that we addressed and briefly discuss before moving to  
304 the case of extrinsic doping is the dependence of the electronic  
305 band gap on the crystal phase. As it is well known, DFT in its  
306 local and semilocal approximation of the exchange–correlation  
307 energy severely underestimates the band gap. Therefore, we  
308 have performed quasiparticle  $G_0W_0$  calculations that allow  
309 bypassing this limitation. The results are reported in Table 1.

310 The electronic properties of bulk ZB GaAs have been  
311 investigated from first principles since decades in view of the  
312 microelectronic-oriented applications of the material<sup>77–80</sup> and  
313 theoretically assessing the band gap of GaAs main polymorphs  
314 remains controversial, as a definitive conclusion is still missing  
315 (see ref 16 for a detailed discussion). Furthermore, although  
316 on one side, there is a large availability of experimental data  
317 about ZB GaAs (see, e.g., refs 81, 82), the scarcity of  
318 experimental data about WZ GaAs samples, mostly derived by  
319 NW structures, makes the comparison with experimental data  
320 for this polymorph a quite cumbersome task because of the  
321 expected overestimation of the gap due to quantum confine-  
322 ment effects. Indeed, there are experimental reports for the  
323 band gap of WZ-GaAs NWs to be either larger or smaller than  
324 the one of ZB-GaAs NWs by few tens of meV.<sup>16</sup>

325 A good description and comparison between DFT- and GW-  
326 calculated electronic properties of the two polymorphs of GaAs  
327 have been provided by Zanolli *et al.*:<sup>83</sup> their LDA-calculated  
328 value for WZ GaAs is 50 meV larger than the ZB-calculated  
329 one, in good agreement with our findings (the absolute values  
330 differ because Zanolli *et al.* used a different, custom-made  
331 pseudopotential<sup>84</sup>) and with those of Yeh *et al.*<sup>78</sup> On the other  
332 hand, the GW values they obtained are 1.133 eV (ZB) and  
333 1.351 eV (WZ), while at the quasiparticle level, we found the

band gap of ZB GaAs to be larger than that of WZ GaAs (see  
Table 1).

A similar problem can be encountered in the case of InP and  
GaP. Because the WZ bulk phase of these compounds is not  
stable under normal conditions, all the experimental data  
concerning its band gap are derived from indirect measure-  
ments on NWs (in which instead the WZ phase can be  
stabilized). The theoretical and experimental literature  
addressing this issue is less extensive when compared to that  
on GaAs. The band gap of WZ InP has been experimentally  
reported to be slightly larger than that of ZB InP (see for  
instance refs 85, 86), in agreement with our results (see Table  
1) and other theoretical calculations.<sup>87</sup> On the other hand, a  
limited number of experiments have been performed to  
investigate the band gap of WZ GaP,<sup>9,26</sup> which is expected to  
be around 2.19 eV. This value is not far from what we  
calculated (2.28 eV) and other *ab initio* quasiparticle  
calculations.<sup>88</sup>

### Impurity Doping: Stability and Transition Energies.

**General Considerations.** Band theory of semiconductors relies  
on a perfect duality between n- and p-type doping, where  
electrons and holes are thermally excited from the impurity  
state to the conduction and valence band. Microscopically,  
however, this duality breaks down because chemical bonds are  
formed by electrons only. Therefore, the case of donors, where  
the four bonds of a tetrahedral semiconductor can be satisfied  
and there is an additional, loosely bound electron, is different  
from the case of acceptors, where the substitutional impurity  
only has three electrons to form bonds.

In the ZB phase, all atoms occupy the center of a perfect  
tetrahedron with all four first neighbor distances equal ( $T_d$   
symmetry). This local symmetry is maintained in the case of  
doping with deformations consisting of the sole uniform  
contraction or expansion of the bond length. In the WZ phase,  
each atom has three equidistant first neighbors, while the  
fourth neighbor, along the  $c$  direction, is usually more far apart  
( $C_{3v}$  symmetry). The WZ structure has thus more structural  
freedom to adjust to perturbations induced by impurities  
because the variations in the bonding can be tuned by the fact  
that there are two different types of bonds. Therefore, when an  
acceptor is introduced in the lattice, it will try to form three  
bonds, something that is favored in the WZ structure where  
three of the bonds can become stronger and one weaker, the  
final outcome being the stabilization of the lattice. This does  
not happen in the ZB lattice. Thus, introducing electron  
deficiency in the pristine III–V solids provides a bias for the  
WZ structure.<sup>53</sup>

Another way of tuning the WZ–ZB stability is by altering  
the ionic component of the bonding. In III–V solids, the bond  
is always partly ionic and one partner is electron-rich, whereas  
the other is electron-poor. Adding electrons or holes has  
different effects: adding electrons increases the electronic  
asymmetry and thus the ionic contribution, whereas adding  
holes decreases the electronic asymmetry and thus the ionic  
contribution. According to the discussion in the previous  
section, an increased ionicity favors the WZ lattice, while more  
covalent bonds favor the ZB. Therefore, adding (removing)  
electrons is expected to stabilize the WZ (ZB) crystal phase.

**Acceptors.** We now move to the discussion of the main  
results of our study and start with impurities that provide p-  
type doping. We computed the formation energies of five  
different systems doped with an acceptor:  $C_{As}@GaAs$ ,  $Si_{As}@$   
 $GaAs$ ,  $Zn_{Ga}@GaAs$ ,  $Zn_{Ga}@GaP$ , and  $Zn_{In}@InP$ , where the

397 notation  $C_{As}@GaAs$  stands for a C atom substituting an As  
 398 atom in a GaAs lattice (and likewise for the other cases). In all  
 399 the cases, we considered the neutral charge state and the  $-1$   
 400 charge state, which is expected to be the more stable charge  
 401 state when the Fermi level lies above the dopant level. These  
 402 are all textbook cases of acceptors, where an atom of the lattice  
 403 is substituted by an impurity from the group of the periodic  
 404 table immediately to its left. Impurities from group-IV can, in  
 405 principle, be both donors and acceptors, depending on the  
 406 sublattice chosen for the substitution.<sup>89</sup> This is the case of Si@  
 407 GaAs, which acts as an acceptor when it substitutes an As atom  
 408 and as a donor when it substitutes a Ga atom. C could behave  
 409 similarly, but substitution at the As sublattice is much more  
 410 stable than substitution at the Ga sublattice (we found a  
 411 difference of 0.27 and 0.37 eV in ZB and WZ GaAs,  
 412 respectively), so the latter in practice never occurs. We recall  
 413 that we carried out our calculations in bulk systems, as an  
 414 approximation of realistic, large-diameter NWs. For a study of  
 415 extrinsic defects in GaAs NWs, the interested reader can see,  
 416 for example, the studies of Galicka *et al.*<sup>90</sup> and Diao *et al.*;<sup>91</sup>  
 417 intrinsic defects in GaAs and their relation with polytypism  
 418 have been explored by Du *et al.*<sup>92</sup>  
 419 The results of the formation energy as a function of the  
 420 chemical potential of the electron for GaAs are shown in  
 421 Figure 2. As it can be seen, all the three acceptors have some

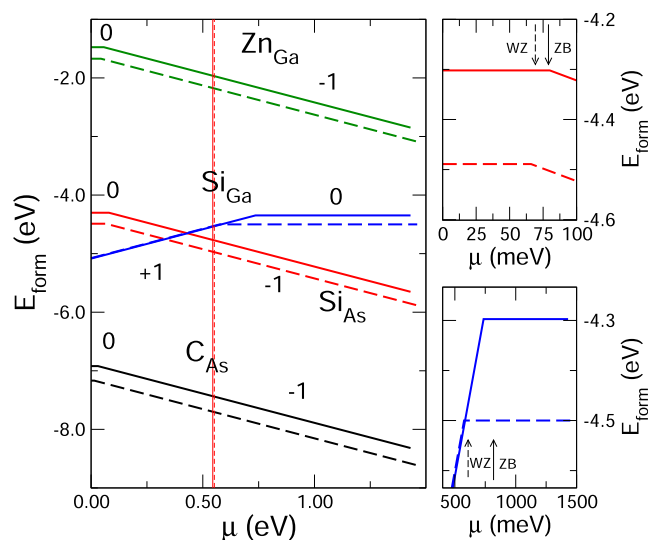


**Figure 2.** Formation energies as a function of the chemical potential of the electron of Si, C, and Zn in ZB (continuous line) and WZ (dashed line) GaAs. The side panels show zoomed-in views of Si<sub>As</sub> (top) and Si<sub>Ga</sub> (bottom).

422 features in common: (i) the neutral impurity is always more  
 423 stable in the WZ lattice, for all values of  $\mu_e$  (see dashed lines in  
 424 Figure 2); (ii) the increased stability is similar in all the cases;  
 425 and (iii) the transition energy is (slightly) smaller in the WZ  
 426 and the impurity state is shallower (see the zoomed view for  
 427 Si<sub>As</sub>@GaAs). Simply put, it is easier to p-type dope GaAs in the  
 428 WZ phase and these dopants will be easier to activate.

429 Following the arguments given above, we now attempt to  
 430 rationalize the observed behavior. A very important factor to  
 431 consider in understanding the role of the impurity is the four  
 432 mismatch between the impurity and the host lattice. The four  
 433 Ga–As bond lengths in pristine WZ GaAs are 2.422 ( $\times 3$ ) and  
 434 2.433 Å. Let us consider the case of Si<sub>As</sub>@GaAs (the full list of

bond lengths is given in the Supporting Information). The Si–  
 435 As bond lengths around the impurity are 2.348 ( $\times 3$ ) and 2.353  
 436 Å, that is, they are all shorter because Si is smaller than As. The  
 437 four distances associated with the four nearest neighbor Ga  
 438 atoms are 2.440–2.430 ( $\times 3$ ) and 2.348–2.353 Å. This means  
 439 that the structural perturbation of the impurity is almost  
 440 limited to the second coordination sphere of the impurity.  
 441 However, more important to notice is the fact that the three  
 442 bonds for every nearest neighbor of the impurity connecting  
 443 with the rest of the GaAs lattice are longer than in the pristine.  
 444 In other words, the stabilizing effect due to the four bonds of  
 445 the Si impurity is at least partially compensated by the  
 446 destabilization of the 12 Ga–As bonds of the second  
 447 coordination sphere. Of course, this effect occurs even more  
 448 intensely for the case of C<sub>As</sub>@GaAs. A different situation  
 449 occurs for Zn<sub>Ga</sub>@GaAs. In that case, the Zn–As distances are  
 450 2.395 ( $\times 3$ ) and 2.397 Å, which are shorter than the initial ones  
 451 but not as much as for Si. However, now, the distances  
 452 connecting the four nearest neighbors with the rest of the  
 453 GaAs lattice are all around 2.390–2.400 Å, that is, they are all  
 454 shorter than the initial ones. Clearly, the better match between  
 455 the impurity and the host lattice allows a weaker but better  
 456 balanced distortion of the lattice, which avoids the above-  
 457 mentioned destabilization of 12 bonds and transforms it into  
 458 stabilization.

459 For all neutral acceptor impurities studied (Table 2), we find  
 460 that whatever the mismatch is, the WZ structure is clearly  
 461

**Table 2.** Difference in the Neutral and Charged Impurity Formation Energy,  $\Delta E_{form}$ , between the ZB and WZ Structures (a Positive Value Indicates That the WZ Is More Stable) for the Series of Acceptor Impurities Studied<sup>a</sup>

	GaAs			GaP	InP
	Si <sub>As</sub>	C <sub>As</sub>	Zn <sub>Ga</sub>	Zn <sub>P</sub>	Zn <sub>P</sub>
$\Delta E_{form}^0$	187	248	197	94	33
$\Delta E_{form}^{-1}$	201	265	210	119	39
$\Delta E(0/-)$	14	17	13	25	6

<sup>a</sup>All energies are given in meV/f.u. We also report the difference in transition energies,  $\Delta E(0/-)$ , between the ZB and WZ structures (a positive value indicates that the impurity state in WZ is shallower).

462 preferred. This is the consequence of two features, both  
 463 already anticipated in the discussion in the previous section:  
 464 (i) acceptor impurities generate electron deficiency in the  
 465 already electron-deficient sites of the lattice and (ii) as far as  
 466 the impurity is smaller or similar in size to the original host  
 467 atom, the induced structural perturbation is more easily  
 468 accommodated within the WZ lattice because of the larger  
 469 structural freedom degrees allowing a 3 + 1-type coordination.  
 470 As shown in Table 2, this preference is even increased for the  
 471 charged impurities. Thus, the transition energies for acceptor  
 472 impurities are always smaller (*i.e.*, the impurity level is closer to  
 473 the valence band,  $\Delta E(0/-)$ , in Table 2) in the WZ structure. If  
 474 we consider impurities in the GaAs lattice, it is clear that the  
 475 increase in the preference when the impurity is charged is an  
 476 almost constant value (the only exception is singly charged Si  
 477 that does not favor any crystal phase). By analyzing the Bader  
 478 charges before and after the charging, we could conclude that  
 479 there is barely any change at the impurity and four nearest  
 480 neighbor sites, thus suggesting that the hole resulting from the  
 481 acceptor impurity must be very delocalized in the lattice.  
 482 Because adding an electron increases the charge asymmetry,

483 the WZ should be further stabilized over the ZB because of the  
 484 charging, although the effect is only modest for acceptor  
 485 impurities. Consequently, our calculations suggest that smaller  
 486 transition energies will be associated with larger stabilizations  
 487 of the WZ structure for the neutral impurity.  
 488 All these considerations are straightforwardly extended to  
 489 the case of  $\text{Zn}_{\text{Ga}}@{\text{GaP}}$  and  $\text{Zn}_{\text{In}}@{\text{InP}}$ , whose formation  
 490 energies are shown in Figures 3 and 4, and thus confirm the  
 491 generality of the trends discussed.

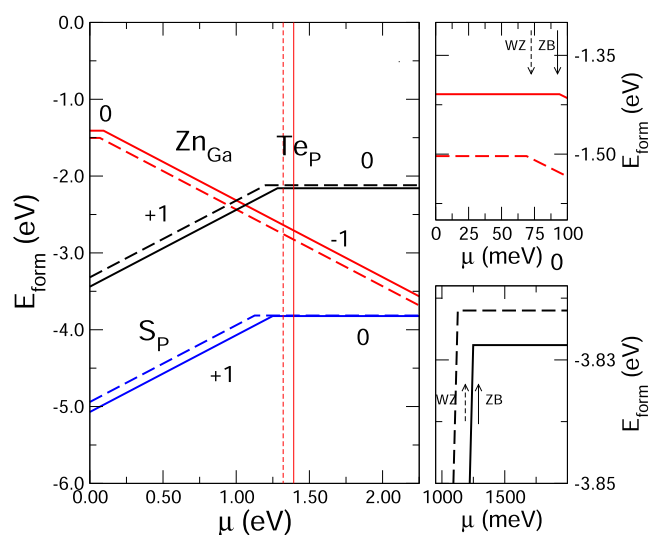


**Figure 3.** Formation energies as a function of the chemical potential of the electron of Te, S, and Zn in ZB (continuous line) and WZ (dashed line) GaP. The side panels show zoomed-in views of  $\text{Zn}_{\text{Ga}}$  (top) and  $\text{Te}_{\text{P}}$  (bottom).

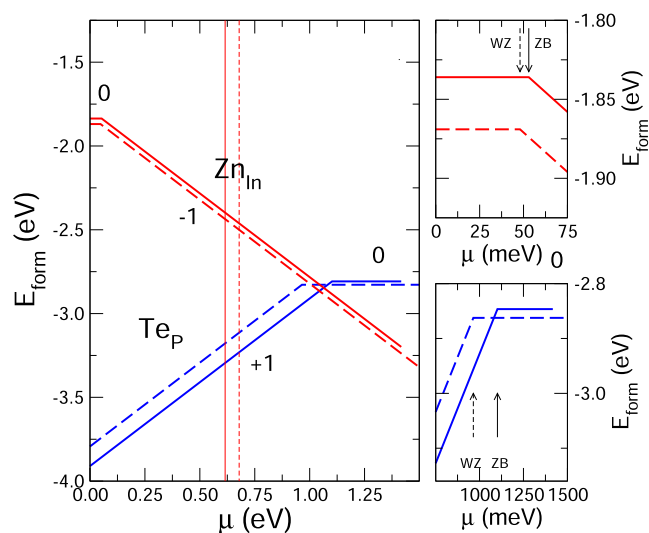


**Figure 4.** Formation energies as a function of the chemical potential of the electron of Te and Zn in ZB (continuous line) and WZ (dashed line) InP. The side panels show zoomed-in views of  $\text{Zn}_{\text{In}}$  (top) and  $\text{Te}_{\text{P}}$  (bottom).

492 **Donors.** We considered four different systems doped with a  
 493 donor:  $\text{Si}_{\text{Ga}}@{\text{GaAs}}$ ,  $\text{S}_{\text{P}}@{\text{GaP}}$ ,  $\text{Te}_{\text{P}}@{\text{GaP}}$ , and  $\text{Te}_{\text{P}}@{\text{InP}}$ . In all  
 494 these cases, an atom of the lattice is substituted by an impurity  
 495 from the group of the periodic table immediately to its right.  
 496 We studied each impurity in the neutral and +1 charge state,  
 497 which is expected to be the more stable charge state when the

Fermi level lies below the dopant level. As mentioned above, Si  
 498 is an amphoteric dopant, so although  $\text{Si}_{\text{As}}@{\text{GaAs}}$  is an  
 499 acceptor, here, we study  $\text{Si}_{\text{Ga}}@{\text{GaAs}}$  that acts as a donor. 500

The results of the formation energy as a function of the  
 501 chemical potential of the electron for the three compounds  
 502 investigated are shown in Figures 2–4. Also, in this case, it is  
 503 possible to highlight some common features: (i) neutral  
 504 chalcogen impurities, S and Te, show no clear preference for  
 505 the ZB or WZ crystal phase; (ii) charged chalcogen impurities  
 506 favor substitution in the ZB structure; and (iii) the transition  
 507 energy is smaller in the ZB, that is, the impurity state is  
 508 shallower (see the zoomed-in view of  $\text{Si}_{\text{Ga}}@{\text{GaAs}}$ ,  $\text{Te}_{\text{P}}@{\text{GaP}}$ ,  
 509 and  $\text{Te}_{\text{P}}@{\text{InP}}$  in the side panels). Therefore, at variance with  
 510 the case of acceptors, donor impurities are more easily  
 511 activated in the ZB crystal phase, while their solubility is  
 512 larger in ZB structures when the impurities are in the +1  
 513 charge state. We note that occasionally, the transition energy  
 514 falls within the conduction band, this being a known  
 515 shortcoming of using LDA to account for the exchange–  
 516 correlation energy and thus of the underestimation of the band  
 517 gap. We have indeed computed much more accurate band gaps  
 518 from  $G_0W_0$  calculations, but treating the doped supercells at  
 519 the same level of the theory is beyond the current  
 520 computational capabilities and, obviously, single-particle and  
 521 many-body results cannot be mixed together. Therefore, the  
 522 conclusions directly related to transition energies obtained  
 523 from DFT–LDA calculations can only be taken to be  
 524 semiquantitative,<sup>59</sup> and approaches that suggest to ignore the  
 525 calculated band edges and reference charge transition levels to  
 526 marker levels<sup>93</sup> or to the average electrostatic potential<sup>94–96</sup>  
 527 have been proposed. We recall once again, however, that our  
 528 main goal is understanding the difference between doping with  
 529 a certain impurity the ZB and WZ crystal phase of a given  
 530 semiconductor and not to quantitatively estimate the transition  
 531 energies. Hence, we argue that all the conclusions based on  
 532 such comparisons are robust and the physical insight they  
 533 provide is reliable. 534

The donors that we studied belong to two different  
 535 categories. When P is substituted by S or Te neutral impurities,  
 536 a structural perturbation different from that discussed above  
 537 takes place. Both atoms are strongly electronegative and  
 538 although they act as donors toward the lattice by generating an  
 539 extra electron, they also gain electron density. For instance, the  
 540 calculated Bader charges for  $\text{S}_{\text{P}}@{\text{GaP}}$  and  $\text{Te}_{\text{P}}@{\text{GaP}}$  are 6.85  
 541 and 6.38  $e^-$ , respectively, in the WZ structure and 6.83 and  
 542 6.42  $e^-$  in the ZB structure (for comparison, the Bader charge  
 543 of P in the pristine GaP lattice amounts to 5.70  $e^-$  in the ZB  
 544 and 5.72  $e^-$  in the WZ; remember that because of the inclusion  
 545 of 3d electrons in the valence of the Ga atom, the total charge  
 546 for each Ga–P pair is 18  $e^-$ ). In fact, this electronic gain  
 547 mostly originates from the polarization of the bonds between  
 548 the very electronegative chalcogen atom and the weakly  
 549 electronegative Ga atom. The important structural observation  
 550 is that in contrast with acceptors, the bonds between the  
 551 chalcogen and the four nearest neighbors become clearly  
 552 longer than in the pristine crystal. For instance, the Ga–P  
 553 bonds in WZ GaP are 2.327 ( $\times 3$ ) and 2.338 Å. The X–Ga (X  
 554 = S and Te) bond lengths around the impurity in  $\text{X}_{\text{P}}@{\text{GaP}}$  are  
 555 as long as 2.407 ( $\times 3$ ) and 2.413 Å for X = S and 2.610 ( $\times 3$ )  
 556 and 2.617 Å for X = Te. The anionic chalcogen atoms, with  
 557 their high electron density, strongly push the four nearest  
 558 neighbor atoms, compressing the lattice around the second  
 559 coordination sphere of the impurity. Under such circum- 560

stances, the additional structural degree of freedom of the WZ structure becomes considerably less effective and the very isotropic nature of the ZB structure becomes comparable or even slightly preferred. Only for the more expanded lattice of InP, the WZ structure is again slightly favored (see Table 3).

**Table 3. Difference in the Neutral and Charged Impurity Formation Energy,  $\Delta E_{\text{form}}$ , between the ZB and WZ Structures (a Positive Value Indicates That the WZ Is More Stable) for the Series of Donor Impurities Studied<sup>a</sup>**

	GaAs	GaP		InP
	Si <sub>Ga</sub>	S <sub>p</sub>	Te <sub>p</sub>	Te <sub>p</sub>
$\Delta E_{\text{form}}^0$	152	-7	-39	20
$\Delta E_{\text{form}}^{+1}$	-8	-130	-122	-117
$\Delta E(+/0)$	160	123	83	137

<sup>a</sup>All energies are given in meV/f.u. We also report the difference in transition energies,  $\Delta E(+/0)$ , between the ZB and WZ structures (a positive value indicates that the impurity state in ZB is shallower).

In contrast, because of the structural mismatch, Si<sub>Ga</sub>@GaAs behaves in the same way described above for the case where Si was acting as an acceptor; the only difference is that the short distances with the four nearest neighbors are now a bit longer (*i.e.*, 2.372 (×3) and 2.382 Å for Si<sub>Ga</sub> compared with 2.348 (×3) and 2.353 Å for Si<sub>As</sub> in GaAs WZ). Thus, according to our calculations, Si in GaAs has a preference for WZ irrespective of acting as a donor or an acceptor. In fact, the calculated energy differences are comparable (187 meV/f.u. for Si<sub>As</sub> and 152 meV/f.u. for Si<sub>Ga</sub>). This result emphasizes the key role of the mismatch in enforcing the WZ–ZB preference.

Note that among the different impurities studied, charging the impurity always favors the ZB structure even when the impurity is smaller than the host atom replaced (Table 3). This contribution is relatively large and finally determines the preference of all donor impurities studied for the ZB structure. We believe the origin of this result is that, as noted above, removing the electron provided by the neutral impurity decreases the ionicity of the lattice and consequently, the ZB structure is favored. According to our calculations, for donors compressing the lattice around the impurity, the shallowness will increase with the size of the impurity and/or decreasing the cell constants of the pristine lattice.

As a final remark, we observe that our computed transition energies, indicating that donor states are shallower in the ZB crystal phase, agree well with the predictions of the hydrogenic model of substitutional impurities within effective mass theory (EMT). Within this simple model, the substitutional impurity form four bonds with the nearest neighbors, with negligible relaxation effects and charge transfer, leaving one unpaired electron whose energy is approximately given by

$$E_n \sim -\text{Ry} \frac{m^*}{\epsilon^2 n^2} \quad (4)$$

where  $m^*$  is the effective mass in units of the electron mass,  $n$  is the main quantum number,  $\epsilon$  is the (relative) static dielectric constant, and Ry is the Rydberg constant. This is the quantum mechanical solution of the hydrogen atom except for the fact that it contains parameters of the bulk host crystal, such as  $m^*$  and  $\epsilon$ .  $E_n$  is the energy of the unpaired electron relative to the conduction band minimum, so large values of  $\epsilon$  and small values of  $m^*$  both contribute to make the impurity shallower,

that is,  $E_n$  small. If we look at the computed values of the static dielectric constant collected in Table 1, we see that for GaAs, GaP, and InP, when going from the ZB to the WZ, it decreases (with a reduction, *i.e.*, slightly more pronounced for the *zz* component of the tensor). As for the electron effective mass, it has been shown experimentally that it is heavier in the WZ than in the ZB,<sup>36,37,97,98</sup> a trend corroborated by our calculations. Therefore, both these effects tend to make the impurity state deeper in the WZ, in agreement with the computed transition energies. EMT also provides an estimate for the effective Bohr radius of the ground state, which is

$$a_B \sim (\epsilon/m^*)a_0 \quad (5)$$

where  $a_0 \sim 0.577$  Å is the Bohr radius of the isolated hydrogen atom. The effective Bohr radius gives a useful indication of the distance over which the dopant wavefunction extends. This value ranges from 0.5 to 11 nm, indicating that the wavefunction can be considerably delocalized and that the donor electron loosely binds to the dopant atom. This observation agrees with the computed Bader charges of the donors that barely change when the system goes from neutral to charged, that is, the additional charge effectively spreads all over the atoms of the supercell.

## CONCLUSIONS

We have presented first-principles density functional calculations of impurity doping in GaAs, GaP, and InP, comparing their stability and transition energies when dopants are introduced in the ZB or in the WZ. The cubic ZB crystal structure is the common crystal phase of bulk arsenides and phosphides, but doping of the WZ is becoming increasingly important because this crystal phase can be stabilized even at room temperature and atmospheric pressure when these semiconductors are grown as NWs. Our results highlight a general trend where acceptors favor substitution in WZ crystals, where they have a shallower electronic state, allowing an easier excitation of charge carriers for band transport. The situation is reversed for donors, which feature a shallower impurity state and higher solubilities in the ZB. These observations are rationalized in terms of the local distortion and electronic charge reorganization upon doping. In particular, we show that (i) the reduced symmetry of the WZ is better suited to accommodate the local relaxation of acceptors, which favors a three-fold coordination and (ii) ionic bonds favor the WZ lattice, while more covalent bonds favor the ZB and the ionic character of the bond can be increased (decreased) by adding electrons (holes). These results are important for the design and optimization of electronic devices based on semiconducting NWs in the growing field of crystal-phase engineering.

## ASSOCIATED CONTENT

### Supporting Information

The Supporting Information is available free of charge at <https://pubs.acs.org/doi/10.1021/acs.jpcc.0c09391>.

First-neighbor distances of the pristine crystal, of the impurity, and of the four first neighbors (PDF)

## AUTHOR INFORMATION

### Corresponding Authors

Enric Canadell – Institut de Ciència de Materials de Barcelona, ICMA-B-CSIC, 08193 Bellaterra, Spain;



664 [orcid.org/0000-0002-4663-5226](https://orcid.org/0000-0002-4663-5226); Email: [canadell@](mailto:canadell@icmab.es)  
665 [icmab.es](mailto:icmab.es)  
666 **Riccardo Rurali** – Institut de Ciència de Materials de  
667 Barcelona, ICMAB-CSIC, 08193 Bellaterra, Spain;  
668 [orcid.org/0000-0002-4086-4191](https://orcid.org/0000-0002-4086-4191); Email: [rrurali@](mailto:rrurali@icmab.es)  
669 [icmab.es](mailto:icmab.es)

## 670 Authors

671 **Giacomo Giorgi** – Department of Civil and Environmental  
672 Engineering, University of Perugia (DICA), 06125 Perugia,  
673 Italy; CNR-SCITEC, 06123 Perugia, Italy; [orcid.org/](https://orcid.org/0000-0003-4892-7908)  
674 [0000-0003-4892-7908](https://orcid.org/0000-0003-4892-7908)  
675 **Michele Amato** – Université Paris-Saclay, CNRS, Laboratoire  
676 de Physique des Solides, 91405 Orsay, France; [orcid.org/](https://orcid.org/0000-0002-3690-3194)  
677 [0000-0002-3690-3194](https://orcid.org/0000-0002-3690-3194)  
678 **Stefano Ossicini** – “Centro S3”, CNR-Istituto di Nanoscienze,  
679 41125 Modena, Italy; Dipartimento di Scienze e Metodi  
680 dell’Ingegneria, Centro Interdipartimentale En&Tech,  
681 Università di Modena e Reggio Emilia, I-42100 Reggio  
682 Emilia, Italy  
683 **Xavier Cartoixà** – Departament d’Enginyeria Electrònica,  
684 Universitat Autònoma de Barcelona, 08193 Bellaterra,  
685 Barcelona, Spain; [orcid.org/0000-0003-1905-5979](https://orcid.org/0000-0003-1905-5979)

686 Complete contact information is available at:

687 <https://pubs.acs.org/10.1021/acs.jpcc.0c09391>

## 688 Author Contributions

689 <sup>V</sup>G.G. and M.A. contributed equally to this work.

## 690 Notes

691 The authors declare no competing financial interest.

## 692 ■ ACKNOWLEDGMENTS

693 We acknowledge financial support by the Ministerio de  
694 Economía, Industria y Competitividad (MINECO) under  
695 grants FEDER-MAT2017-90024-P and PGC2018-096955-B-  
696 C44, the Severo Ochoa Centres of Excellence Program under  
697 grant SEV-2015-0496, and the Generalitat de Catalunya under  
698 grants no. 2017 SGR 1506. We thank the Centro de  
699 Supercomputación de Galicia (CESGA) for the use of their  
700 computational resources. M.A. acknowledges the ANR  
701 HEXSIGE project (ANR-17-CE030-0014-01) of the French  
702 Agence Nationale de la Recherche. Part of the high-  
703 performance computing resources for this project were granted  
704 by the Institut du développement et des ressources en  
705 informatique scientifique (IDRIS) under the allocation  
706 A0040910089 via GENCI (Grand Equipement National de  
707 Calcul Intensif). S.O. acknowledges support/funding from the  
708 University of Modena and Reggio Emilia under project  
709 “FAR2017INTERDISC” G.G. acknowledges PRACE for  
710 awarding the access to the Marconi system based in Italy at  
711 CINECA and the Italian ISCRA program.

## 712 ■ REFERENCES

713 (1) Wang, N.; Cai, Y.; Zhang, R. Q. Growth of nanowires. *Mater. Sci.*  
714 *Eng., R* **2008**, *60*, 1–51.  
715 (2) Schmidt, V.; Wittemann, J. V.; Senz, S.; Gösele, U. Silicon  
716 Nanowires: A Review on Aspects of their Growth and their Electrical  
717 Properties. *Adv. Mater.* **2009**, *21*, 2681–2702.  
718 (3) Caroff, P.; Bolinsson, J.; Johansson, J. Crystal Phases in III–V  
719 Nanowires: From Random Toward Engineered Polytypism. *IEEE J.*  
720 *Sel. Top. Quantum Electron.* **2011**, *17*, 829–846.  
721 (4) Koguchi, M.; Kakibayashi, H.; Yazawa, M.; Hiruma, K.;  
722 Katsuyama, T. Crystal Structure Change of GaAs and InAs Whiskers

from Zinc-Blende to Wurtzite Type. *Jpn. J. Appl. Phys., Part 1* **1992**, *723*  
*31*, 2061. 724  
(5) Persson, A. I.; Larsson, M. W.; Stenström, S.; Ohlsson, B. J.;  
725 Samuelson, L.; Wallenberg, L. R. Solid-phase diffusion mechanism for  
726 GaAs nanowire growth. *Nat. Mater.* **2004**, *3*, 677–681. 727  
(6) Harmand, J. C.; Patriarche, G.; Péré-Laperme, N.; Mérat-  
728 Combes, M.-N.; Travers, L.; Glas, F. Analysis of vapor-liquid-solid  
729 mechanism in Au-assisted GaAs nanowire growth. *Appl. Phys. Lett.* **730**  
**2005**, *87*, 203101. 731  
(7) Funk, S.; Li, A.; Ercolani, D.; Gemmi, M.; Sorba, L.; Zardo, I.  
732 Crystal Phase Induced Bandgap Modifications in AlAs Nanowires  
733 Probed by Resonant Raman Spectroscopy. *ACS Nano* **2013**, *7*, 1400–  
734 1407. 735  
(8) Mohan, P.; Motohisa, J.; Fukui, T. Controlled growth of highly  
736 uniform, axial/radial direction-defined, individually addressable InP  
737 nanowire arrays. *Nanotechnology* **2005**, *16*, 2903. 738  
(9) Assali, S.; Zardo, I.; Plissard, S.; Kriegner, D.; Verheijen, M. A.;  
739 Bauer, G.; Meijerink, A.; Belabbes, A.; Bechstedt, F.; Haverkort, J. E.  
740 M.; Bakkers, E. P. A. M. Direct Band Gap Wurtzite Gallium  
741 Phosphide Nanowires. *Nano Lett.* **2013**, *13*, 1559–1563. 742  
(10) Vu, T. T. T.; Zehender, T.; Verheijen, M. A.; Plissard, S. R.;  
743 Immink, G. W. G.; Haverkort, J. E. M.; Bakkers, E. P. A. M. High  
744 optical quality single crystal phase wurtzite and zincblende InP  
745 nanowires. *Nanotechnology* **2013**, *24*, 115705. 746  
(11) Lehmann, S.; Wallentin, J.; Mårtensson, E. K.; Ek, M.;  
747 Deppert, K.; Dick, K. A.; Borgström, M. T. Simultaneous Growth of  
748 Pure Wurtzite and Zinc Blende Nanowires. *Nano Lett.* **2019**, *19*,  
749 2723–2730. 750  
(12) Vincent, L.; Patriarche, G.; Hallais, G.; Renard, C.; Gardès, C.;  
751 Troadec, D.; Bouchier, D. Novel Heterostructured Ge Nanowires  
752 Based on Polytype Transformation. *Nano Lett.* **2014**, *14*, 4828–4836. 753  
(13) Hauge, H. I. T.; Verheijen, M. A.; Conesa-Boj, S.; Etzelstorfer,  
754 T.; Watzinger, M.; Kriegner, D.; Zardo, I.; Fasolato, C.; Capitani, F.;  
755 Postorino, P.; Kölling, S.; Li, A.; Assali, S.; Stangl, J.; Bakkers, E. P. A.  
756 M. Hexagonal Silicon Realized. *Nano Lett.* **2015**, *15*, 5855–5860. 757  
(14) Hauge, H. I. T.; Conesa-Boj, S.; Verheijen, M. A.; Koelling, S.;  
758 Bakkers, E. P. A. M. Single-Crystalline Hexagonal Silicon-Germanium.  
759 *Nano Lett.* **2017**, *17*, 85–90. 760  
(15) Vincent, L.; Djomani, D.; Fakfakh, M.; Renard, C.; Belier, B.;  
761 Bouchier, D.; Patriarche, G. Shear-driven phase transformation in  
762 silicon nanowires. *Nanotechnology* **2018**, *29*, 125601. 763  
(16) Tizei, L. H. G.; Amato, M. Electronic structure and optical  
764 properties of semiconductor nanowires polytypes. *Eur. Phys. J. B* **765**  
**2020**, *93*, 16. 766  
(17) Cartoixà, X.; Palummo, M.; Hauge, H. I. T.; Bakkers, E. P. A.  
767 M.; Rurali, R. Optical Emission in Hexagonal SiGe Nanowires. *Nano*  
768 *Lett.* **2017**, *17*, 4753–4758. 769  
(18) Fadaly, E. M. T.; Dijkstra, A.; Suckert, J. R.; Ziss, D.; van  
770 Tilburg, M. A. J.; Mao, C.; Ren, Y.; van Lange, V. T.; Korzun, K.;  
771 Kölling, S.; et al. Direct-bandgap emission from hexagonal Ge and  
772 SiGe alloys. *Nature* **2020**, *580*, 205–209. 773  
(19) Zardo, I.; Yazji, S.; Hörmann, N.; Hertenberger, S.; Funk, S.;  
774 Mangialardo, S.; Morkötter, S.; Koblmüller, G.; Postorino, P.;  
775 Abstreiter, G. E1(A) Electronic Band Gap in Wurtzite InAs  
776 Nanowires Studied by Resonant Raman Scattering. *Nano Lett.* **777**  
**2013**, *13*, 3011–3016. 778  
(20) De Luca, M.; Polimeni, A. Electronic properties of wurtzite-  
779 phase InP nanowires determined by optical and magneto-optical  
780 spectroscopy. *Appl. Phys. Rev.* **2017**, *4*, 041102. 781  
(21) Senichev, A.; Corfdir, P.; Brandt, O.; Ramsteiner, M.; Breuer,  
782 S.; Schilling, J.; Geelhaar, L.; Werner, P. Electronic properties of  
783 wurtzite GaAs: A correlated structural, optical, and theoretical analysis  
784 of the same polytypic GaAs nanowire. *Nano Res.* **2018**, *11*, 4708–  
785 4721. 786  
(22) Spirkoska, D.; Arbiol, J.; Gustafsson, A.; Conesa-Boj, S.; Glas,  
787 F.; Zardo, I.; Heigoldt, M.; Gass, M. H.; Bleloch, A. L.; Estrade, S.;  
788 et al. Structural and optical properties of high quality zinc-blende/  
789 wurtzite GaAs nanowire heterostructures. *Phys. Rev. B: Condens.* **790**  
*Matter Mater. Phys.* **2009**, *80*, 245325. 791

- 792 (23) Heiss, M.; Conesa-Boj, S.; Ren, J.; Tseng, H.-H.; Gali, A.;  
793 Rudolph, A.; Uccelli, E.; Peiró, F.; Morante, J. R.; Schuh, D.; Reiger,  
794 E.; Kaxiras, E.; Arbiol, J.; Fontcuberta i Morral, A. Direct correlation  
795 of crystal structure and optical properties in wurtzite/zinc-blende  
796 GaAs nanowire heterostructures. *Phys. Rev. B: Condens. Matter Mater.*  
797 *Phys.* **2011**, *83*, 045303.
- 798 (24) De Luca, M.; Zilli, A.; Fonseka, H. A.; Mokkaapati, S.;  
799 Miriametro, A.; Tan, H. H.; Smith, L. M.; Jagadish, C.; Capizzi, M.;  
800 Polimeni, A. Polarized Light Absorption in Wurtzite InP Nanowire  
801 Ensembles. *Nano Lett.* **2015**, *15*, 998–1005.
- 802 (25) Zilli, A.; De Luca, M.; Tedeschi, D.; Fonseka, H. A.;  
803 Miriametro, A.; Tan, H. H.; Jagadish, C.; Capizzi, M.; Polimeni, A.  
804 Temperature Dependence of Interband Transitions in Wurtzite InP  
805 Nanowires. *ACS Nano* **2015**, *9*, 4277–4287.
- 806 (26) Assali, S.; Greil, J.; Zardo, I.; Belabbes, A.; de Moor, M. W. A.;  
807 Koelling, S.; Koenraad, P. M.; Bechstedt, F.; Bakkers, E. P. A. M.;  
808 Haverkort, J. E. M. Optical study of the band structure of wurtzite  
809 GaP nanowires. *J. Appl. Phys.* **2016**, *120*, 044304.
- 810 (27) Zardo, I.; Conesa-Boj, S.; Peiro, F.; Morante, J. R.; Arbiol, J.;  
811 Uccelli, E.; Abstreiter, G.; Fontcuberta i Morral, A. Raman  
812 spectroscopy of wurtzite and zinc-blende GaAs nanowires: Polar-  
813 ization dependence, selection rules, and strain effects. *Phys. Rev. B:*  
814 *Condens. Matter Mater. Phys.* **2009**, *80*, 245324.
- 815 (28) Raya-Moreno, M.; Aramberri, H.; Seijas-Bellido, J. A.; Cartoixa,  
816 X.; Rurali, R. Thermal conductivity of hexagonal Si and hexagonal Si  
817 nanowires from first-principles. *Appl. Phys. Lett.* **2017**, *111*, 032107.
- 818 (29) Raya-Moreno, M.; Rurali, R.; Cartoixa, X. Thermal conductivity  
819 for III-V and II-VI semiconductor wurtzite and zinc-blende polytypes:  
820 The role of anharmonicity and phase space. *Phys. Rev. Mater.* **2019**, *3*,  
821 084607.
- 822 (30) Fasolato, C.; De Luca, M.; Djomani, D.; Vincent, L.; Renard,  
823 C.; Di Iorio, G.; Paillard, V.; Amato, M.; Rurali, R.; Zardo, I.  
824 Crystalline, Phononic, and Electronic Properties of Heterostructured  
825 Polytypic Ge Nanowires by Raman Spectroscopy. *Nano Lett.* **2018**,  
826 *18*, 7075–7084.
- 827 (31) de Matteis, D.; De Luca, M.; Fadaly, E. M. T.; Verheijen, M. A.;  
828 López-Suárez, M.; Rurali, R.; Bakkers, E. P. A. M.; Zardo, I. Probing  
829 Lattice Dynamics and Electronic Resonances in Hexagonal Ge and  
830 Si<sub>x</sub>Ge<sub>1-x</sub> Alloys in Nanowires by Raman Spectroscopy. *ACS Nano*  
831 **2020**, *14*, 6845–6856.
- 832 (32) Glas, F.; Harmand, J.-C.; Patriarche, G. Why Does Wurtzite  
833 Form in Nanowires of III-V Zinc Blende Semiconductors? *Phys. Rev.*  
834 *Lett.* **2007**, *99*, 146101.
- 835 (33) Dubrovskii, V. G.; Sibirev, N. V.; Harmand, J. C.; Glas, F.  
836 Growth kinetics and crystal structure of semiconductor nanowires.  
837 *Phys. Rev. B: Condens. Matter Mater. Phys.* **2008**, *78*, 235301.
- 838 (34) Dubrovskii, V. G.; Sibirev, N. V. Growth thermodynamics of  
839 nanowires and its application to polytypism of zinc blende III-V  
840 nanowires. *Phys. Rev. B: Condens. Matter Mater. Phys.* **2008**, *77*,  
841 035414.
- 842 (35) Zheng, H.; Wang, J.; Huang, J. Y.; Wang, J.; Zhang, Z.; Mao, S.  
843 X. Dynamic Process of Phase Transition from Wurtzite to Zinc  
844 Blende Structure in InAs Nanowires. *Nano Lett.* **2013**, *13*, 6023–  
845 6027.
- 846 (36) Corfdir, P.; Van Hattem, B.; Uccelli, E.; Conesa-Boj, S.;  
847 Lefebvre, P.; Fontcuberta i Morral, A.; Phillips, R. T. Three-  
848 Dimensional Magneto-Photoluminescence as a Probe of the  
849 Electronic Properties of Crystal-Phase Quantum Disks in GaAs  
850 Nanowires. *Nano Lett.* **2013**, *13*, 5303–5310.
- 851 (37) Tedeschi, D.; Fonseka, H. A.; Blundo, E.; del Águila, A. G.;  
852 Guo, Y.; Tan, H. H.; Christianen, P. C. M.; Jagadish, C.; Polimeni, A.;  
853 De Luca, M. Hole and Electron Effective Masses in Single InP  
854 Nanowires with a Wurtzite-Zincblende Homo Junction. *ACS Nano*  
855 **2020**, *14*, 11613–11622.
- 856 (38) Caroff, P.; Dick, K. A.; Johansson, J.; Messing, M. E.; Deppert,  
857 K.; Samuelson, L. Controlled polytypic and twin-plane superlattices in  
858 III–V nanowires. *Nat. Nanotechnol.* **2009**, *4*, 50–55.
- (39) Dick, K. A.; Thelander, C.; Samuelson, L.; Caroff, P. Crystal  
Phase Engineering in Single InAs Nanowires. *Nano Lett.* **2010**, *10*,  
3494–3499.
- (40) Algra, R. E.; Verheijen, M. A.; Borgström, M. T.; Feiner, L.-F.;  
Immink, G.; van Enckevort, W. J. P.; Vlieg, E.; Bakkers, E. P. A. M.  
Twinning superlattices in indium phosphide nanowires. *Nature* **2008**,  
456, 369–372.
- (41) Burgess, T.; Breuer, S.; Caroff, P.; Wong-Leung, J.; Gao, Q.;  
Tan, H. H.; Jagadish, C. Twinning Superlattice Formation in GaAs  
Nanowires. *ACS Nano* **2013**, *7*, 8105–8114.
- (42) Zhang, L.; Luo, J.-W.; Zunger, A.; Akopian, N.; Zwiller, V.;  
Harmand, J.-C. Wide InP Nanowires with Wurtzite/Zincblende  
Superlattice Segments Are Type-II whereas Narrower Nanowires  
Become Type-I: An Atomistic Pseudopotential Calculation. *Nano*  
*Lett.* **2010**, *10*, 4055–4060.
- (43) Amato, M.; Kaewmaraya, T.; Zobelli, A.; Palummo, M.; Rurali,  
R. Crystal Phase Effects in Si Nanowire Polytypes and Their  
Homojunctions. *Nano Lett.* **2016**, *16*, 5694–5700.
- (44) De Luca, M.; Fasolato, C.; Verheijen, M. A.; Ren, Y.; Swinkels,  
M. Y.; Kölling, S.; Bakkers, E. P. A. M.; Rurali, R.; Cartoixa, X.; Zardo,  
I. Phonon Engineering in Twinning Superlattice Nanowires. *Nano*  
*Lett.* **2019**, *19*, 4702–4711.
- (45) Carrete, J.; López-Suárez, M.; Raya-Moreno, M.; Bochkarev, A.  
S.; Royo, M.; Madsen, G. K. H.; Cartoixa, X.; Mingo, N.; Rurali, R.  
Phonon transport across crystal-phase interfaces and twin boundaries  
in semiconducting nanowires. *Nanoscale* **2019**, *11*, 16007–16016.
- (46) Corfdir, P.; Lewis, R. B.; Marquardt, O.; Küpers, H.; Grandal,  
J.; Dimakis, E.; Trampert, A.; Geelhaar, L.; Brandt, O.; Phillips, R. T.  
Exciton recombination at crystal-phase quantum rings in GaAs/  
In<sub>x</sub>Ga<sub>1-x</sub>As core/multishell nanowires. *Appl. Phys. Lett.* **2016**, *109*,  
082107.
- (47) Royo, M.; De Luca, M.; Rurali, R.; Zardo, I. A review on III-V  
core-multishell nanowires: growth, properties, and applications. *J.*  
*Phys. D: Appl. Phys.* **2017**, *50*, 143001.
- (48) Kresse, G.; Furthmüller, J. Efficient iterative schemes for ab  
initio total-energy calculations using a plane-wave basis set. *Phys. Rev.*  
*B: Condens. Matter Mater. Phys.* **1996**, *54*, 11169.
- (49) Blöchl, P. E. Projector augmented-wave method. *Phys. Rev. B:*  
*Condens. Matter Mater. Phys.* **1994**, *50*, 17953.
- (50) Kresse, G.; Joubert, D. From ultrasoft pseudopotentials to the  
projector augmented-wave method. *Phys. Rev. B: Condens. Matter*  
*Mater. Phys.* **1999**, *59*, 1758.
- (51) El-Mellouhi, F.; Mousseau, N.; Ordejón, P. Sampling the  
diffusion paths of a neutral vacancy in silicon with quantum  
mechanical calculations. *Phys. Rev. B: Condens. Matter Mater. Phys.*  
**2004**, *70*, 205202.
- (52) Sholihun; Ishii, F.; Saito, M. First-principles calculations of  
multivacancies in germanium. *Jpn. J. Appl. Phys.* **2016**, *55*, 011301.
- (53) Amato, M.; Ossicini, S.; Canadell, E.; Rurali, R. Preferential  
Positioning, Stability, and Segregation of Dopants in Hexagonal Si  
Nanowires. *Nano Lett.* **2019**, *19*, 866–876.
- (54) Amato, M.; Kaewmaraya, T.; Zobelli, A. Extrinsic Doping in  
Group IV Hexagonal-Diamond-Type Crystals. *J. Phys. Chem. C* **2020**,  
*124*, 17290–17298.
- (55) Leslie, M.; Gillan, N. J. The energy and elastic dipole tensor of  
defects in ionic crystals calculated by the supercell method. *J. Phys. C:*  
*Solid State Phys.* **1985**, *18*, 973–982.
- (56) Makov, G.; Payne, M. C. Periodic boundary conditions in ab  
initio calculations. *Phys. Rev. B: Condens. Matter Mater. Phys.* **1995**, *51*,  
4014–4022.
- (57) Freysoldt, C.; Neugebauer, J.; de Walle, C. G. V. Fully Ab Initio  
Finite-Size Corrections for Charged-Defect Supercell Calculations.  
*Phys. Rev. Lett.* **2009**, *102*, 016402.
- (58) Freysoldt, C.; Neugebauer, J.; Van de Walle, C. G. Electrostatic  
interactions between charged defects in supercells. *Phys. Status Solidi*  
*B* **2011**, *248*, 1067–1076.
- (59) Freysoldt, C.; Grabowski, B.; Hickel, T.; Neugebauer, J.;  
Kresse, G.; Janotti, A.; Van de Walle, C. G. First-principles 926

- 927 calculations for point defects in solids. *Rev. Mod. Phys.* **2014**, *86*, 253–  
928 305.
- 929 (60) Ziman, J. M. *Principles of the Theory of Solids*, 2nd ed.;  
930 Cambridge University Press, 1972; pp 37–41.
- 931 (61) Ewald, P. P. Die Berechnung optischer und elektrostatischer  
932 Gitterpotentiale. *Ann. Phys.* **1921**, *369*, 253–287.
- 933 (62) Rurali, R.; Cartoixà, X. Theory of Defects in One-Dimensional  
934 Systems: Application to Al-Catalyzed Si Nanowires. *Nano Lett.* **2009**,  
935 *9*, 975–979.
- 936 (63) Rurali, R.; Palumbo, M.; Cartoixà, X. Convergence study of  
937 neutral and charged defect formation energies in Si nanowires. *Phys.*  
938 *Rev. B: Condens. Matter Mater. Phys.* **2010**, *81*, 235304.
- 939 (64) Zhang, S.; Northrup, J. Chemical potential dependence of  
940 defect formation energies in GaAs: Application to Ga self-diffusion.  
941 *Phys. Rev. Lett.* **1991**, *67*, 2339–2342.
- 942 (65) Northrup, J. E.; Zhang, S. B. Dopant and defect energetics: Si in  
943 GaAs. *Phys. Rev. B: Condens. Matter Mater. Phys.* **1993**, *47*, 6791–  
944 6794.
- 945 (66) Van de Walle, C. G. Energies of various configurations of  
946 hydrogen in silicon. *Phys. Rev. B: Condens. Matter Mater. Phys.* **1994**,  
947 *49*, 4579–4585.
- 948 (67) Van de Walle, C. G.; Laks, D. B.; Neumark, G. F.; Pantelides, S.  
949 T. First-principles calculations of solubilities and doping limits: Li, Na,  
950 and N in ZnSe. *Phys. Rev. B: Condens. Matter Mater. Phys.* **1993**, *47*,  
951 9425–9434.
- 952 (68) Luo, X.; Zhang, S. B.; Wei, S.-H. Theory of Mn supersaturation  
953 in Si and Ge. *Phys. Rev. B: Condens. Matter Mater. Phys.* **2004**, *70*,  
954 033308.
- 955 (69) Fahey, P. M.; Griffin, P. B.; Plummer, J. D. Point defects and  
956 dopant diffusion in silicon. *Rev. Mod. Phys.* **1989**, *61*, 289–384.
- 957 (70) Stumpf, R.; Scheffler, M. Theory of self-diffusion at and growth  
958 of Al(111). *Phys. Rev. Lett.* **1994**, *72*, 254–257.
- 959 (71) Aradi, B.; Gali, A.; Deák, P.; Lowther, J. E.; Son, N. T.; Janzén,  
960 E.; Choyke, W. J. Ab initio density-functional supercell calculations of  
961 hydrogen defects in cubic SiC. *Phys. Rev. B: Condens. Matter Mater.*  
962 *Phys.* **2001**, *63*, 245202.
- 963 (72) Yeh, C.-Y.; Lu, Z. W.; Froyen, S.; Zunger, A. Zinc-blende–  
964 wurtzite polytypism in semiconductors. *Phys. Rev. B: Condens. Matter*  
965 *Mater. Phys.* **1992**, *46*, 10086–10097.
- 966 (73) Ito, T. Simple Criterion for Wurtzite-Zinc-Blende Polytypism  
967 in Semiconductors. *Jpn. J. Appl. Phys., Part 1* **1998**, *37*, L1217–L1220.
- 968 (74) García, A.; Cohen, M. L. First-principles ionicity scales. I.  
969 Charge asymmetry in the solid state. *Phys. Rev. B: Condens. Matter*  
970 *Mater. Phys.* **1993**, *47*, 4215–4220.
- 971 (75) García, A.; Cohen, M. L. First-principles ionicity scales. II.  
972 Structural coordinates from atomic calculations. *Phys. Rev. B: Condens.*  
973 *Matter Mater. Phys.* **1993**, *47*, 4221–4225.
- 974 (76) Abu-Farsakh, H.; Qteish, A. Ionicity scale based on the centers  
975 of maximally localized Wannier functions. *Phys. Rev. B: Condens.*  
976 *Matter Mater. Phys.* **2007**, *75*, 085201.
- 977 (77) Wei, S.-H.; Zunger, A. Predicted band-gap pressure coefficients  
978 of all diamond and zinc-blende semiconductors: Chemical trends.  
979 *Phys. Rev. B: Condens. Matter Mater. Phys.* **1999**, *60*, 5404–5411.
- 980 (78) Yeh, C.-Y.; Wei, S.-H.; Zunger, A. Relationships between the  
981 band gaps of the zinc-blende and wurtzite modifications of  
982 semiconductors. *Phys. Rev. B: Condens. Matter Mater. Phys.* **1994**,  
983 *50*, 2715–2718.
- 984 (79) Lany, S.; Zunger, A. Assessment of correction methods for the  
985 band-gap problem and for finite-size effects in supercell defect  
986 calculations: Case studies for ZnO and GaAs. *Phys. Rev. B: Condens.*  
987 *Matter Mater. Phys.* **2008**, *78*, 235104.
- 988 (80) Giorgi, G.; Schilfgarde, M.; Korkin, A.; Yamashita, K. On the  
989 Chemical Origin of the Gap Bowing in (GaAs)<sub>1-x</sub>Ge<sub>x</sub> Alloys: A  
990 Combined DFT-QSGW Study. *Nanoscale Res. Lett.* **2010**, *5*, 469–  
991 477.
- 992 (81) Ley, L.; Pollak, R. A.; McFeely, F. R.; Kowalczyk, S. P.; Shirley,  
993 D. A. Total valence-band densities of states of III-V and II-VI  
994 compounds from x-ray photoemission spectroscopy. *Phys. Rev. B:*  
995 *Solid State* **1974**, *9*, 600–621.
- (82) Lautenschlager, P.; Garriga, M.; Logothetidis, S.; Cardona, M. 996  
Interband critical points of GaAs and their temperature dependence. 997  
*Phys. Rev. B: Condens. Matter Mater. Phys.* **1987**, *35*, 9174–9189. 998
- (83) Zanolli, Z.; Fuchs, F.; Furthmüller, J.; von Barth, U.; Bechstedt, 999  
F. Model GW band structure of InAs and GaAs in the wurtzite phase. 1000  
*Phys. Rev. B: Condens. Matter Mater. Phys.* **2007**, *75*, 245121. 1001
- (84) Zanolli, Z. Private communication. 1002
- (85) Tedeschi, D.; De Luca, M.; del Águila, A. G.; Gao, Q.; 1003  
Ambrosio, G.; Capizzi, M.; Tan, H. H.; Christianen, P. C. M.; 1004  
Jagadish, C.; Polimeni, A. Value and anisotropy of the electron and 1005  
hole mass in pure wurtzite InP nanowires. *Nano Lett.* **2016**, *16*, 6213– 1006  
6221. 1007
- (86) Mishra, A.; Titova, L. V.; Hoang, T. B.; Jackson, H. E.; Smith, 1008  
L. M.; Yarrison-Rice, J. M.; Kim, Y.; Joyce, H. J.; Gao, Q.; Tan, H. H.; 1009  
Jagadish, C. Polarization and temperature dependence of photo- 1010  
luminescence from zincblende and wurtzite InP nanowires. *Appl. Phys.* 1011  
*Lett.* **2007**, *91*, 263104. 1012
- (87) Belabbes, A.; Panse, C.; Furthmüller, J.; Bechstedt, F. Electronic 1013  
bands of III-V semiconductor polytypes and their alignment. *Phys.* 1014  
*Rev. B: Condens. Matter Mater. Phys.* **2012**, *86*, 075208. 1015
- (88) Belabbes, A.; Bechstedt, F. Forbidden Band-Edge Excitons of 1016  
Wurtzite-GaP: A Theoretical View. *Phys. Status Solidi B* **2019**, *256*, 1017  
1800238. 1018
- (89) Giorgi, G.; Yamashita, K. Amphoteric behavior of Ge in GaAs: 1019  
an LDA analysis. *Modell. Simul. Mater. Sci. Eng.* **2011**, *19*, 035001. 1020
- (90) Galicka, M.; Buczko, R.; Kacman, P. Segregation of Impurities 1021  
in GaAs and InAs Nanowires. *J. Phys. Chem. C* **2013**, *117*, 20361– 1022  
20370. 1023
- (91) Diao, Y.; Liu, L.; Xia, S. Exploration the p-type doping 1024  
mechanism of GaAs nanowires from first-principles study. *Phys. Lett.* 1025  
*A* **2019**, *383*, 202–209. 1026
- (92) Du, Y. A.; Sakong, S.; Kratzer, P. As vacancies, Ga antisites, and 1027  
Au impurities in zinc blende and wurtzite GaAs nanowire segments 1028  
from first principles. *Phys. Rev. B: Condens. Matter Mater. Phys.* **2013**, 1029  
*87*, 075308. 1030
- (93) Coutinho, J.; Torres, V. J. B.; Jones, R.; Briddon, P. R. Electrical 1031  
activity of chalcogen-hydrogen defects in silicon. *Phys. Rev. B:* 1032  
*Condens. Matter Mater. Phys.* **2003**, *67*, 035205. 1033
- (94) Alkauskas, A.; Broqvist, P.; Pasquarello, A. Defect Energy 1034  
Levels in Density Functional Calculations: Alignment and Band Gap 1035  
Problem. *Phys. Rev. Lett.* **2008**, *101*, 046405. 1036
- (95) Komsa, H.-P.; Broqvist, P.; Pasquarello, A. Alignment of defect 1037  
levels and band edges through hybrid functionals: Effect of screening 1038  
in the exchange term. *Phys. Rev. B: Condens. Matter Mater. Phys.* **2010**, 1039  
*81*, 205118. 1040
- (96) Alkauskas, A.; Pasquarello, A. Band-edge problem in the 1041  
theoretical determination of defect energy levels: The O vacancy in 1042  
ZnO as a benchmark case. *Phys. Rev. B: Condens. Matter Mater. Phys.* 1043  
**2011**, *84*, 125206. 1044
- (97) Graham, A. M.; Corfdir, P.; Heiss, M.; Conesa-Boj, S.; Uccelli, 1045  
E.; Fontcuberta i Morral, A.; Phillips, R. T. Exciton localization 1046  
mechanisms in wurtzite/zinc-blende GaAs nanowires. *Phys. Rev. B:* 1047  
*Condens. Matter Mater. Phys.* **2013**, *87*, 125304. 1048
- (98) De Luca, M.; Rubini, S.; Felici, M.; Meaney, A.; Christianen, P. 1049  
C. M.; Martelli, F.; Polimeni, A. Addressing the Fundamental 1050  
Electronic Properties of Wurtzite GaAs Nanowires by High-Field 1051  
Magneto-Photoluminescence Spectroscopy. *Nano Lett.* **2017**, *17*, 1052  
6540–6547. 1053